



HAL
open science

Structure and Elasticity of Mitochondrial Membranes: A Molecular Dynamics Simulation Study

Thi Ly Mai, Philippe Derreumaux, Phuong H Nguyen

► **To cite this version:**

Thi Ly Mai, Philippe Derreumaux, Phuong H Nguyen. Structure and Elasticity of Mitochondrial Membranes: A Molecular Dynamics Simulation Study. *Journal of Physical Chemistry B*, In press, 10.1021/acs.jpcc.3c05112 . hal-04338565

HAL Id: hal-04338565

<https://hal.science/hal-04338565>

Submitted on 12 Dec 2023

HAL is a multi-disciplinary open access archive for the deposit and dissemination of scientific research documents, whether they are published or not. The documents may come from teaching and research institutions in France or abroad, or from public or private research centers.

L'archive ouverte pluridisciplinaire **HAL**, est destinée au dépôt et à la diffusion de documents scientifiques de niveau recherche, publiés ou non, émanant des établissements d'enseignement et de recherche français ou étrangers, des laboratoires publics ou privés.

Structure and elasticity of mitochondrial membranes: a molecular dynamics simulation study

Thi Ly Mai¹, Philippe Derreumaux^{1,2}, Phuong H. Nguyen^{1*}

¹*CNRS, Université Paris Cité, UPR9080, Laboratoire de Biochimie Théorique, Institut de Biologie Physico-Chimique, Fondation Edmond de Rothschild, 13 rue Pierre et Marie Curie, 75005 Paris, France*

²*Institut Universitaire de France (IUF), 75005, Paris, France*

Abstract

Mitochondria are known as the powerhouse of the cell because they produce energy in the form of ATP. They also have other crucial functions such as regulating apoptosis, calcium homeostasis, and reactive oxygen species production. To carry out these diverse functions, mitochondria adopt specific structures and frequently undergo dynamic shape changes, indicating that their mechanical properties play an essential role in their functions. To gain a detailed understanding at the molecular level of the structure and mechanical properties of mitochondria, we carry out atomistic molecular dynamics simulations for three inner mitochondrial membrane and three outer mitochondrial membrane models. These models take into account variations in cardiolipin and cholesterol concentrations, as well as the symmetry/asymmetry between the two leaflets. Our simulations allow us to calculate various structural quantities and the bending, twist, and tilt elastic moduli of the membrane models. Our results indicate that the structure of the inner and outer mitochondrial membranes is quite similar and does not depend much on the variation in lipid compositions. However, the bending modulus of the membranes increases with increasing concentrations of cardiolipin or cholesterol, but decreases with membrane asymmetry. Notably, we found that the dipole potential of the membrane increases with increasing cardiolipin concentration. Finally, possible roles of cardiolipin in regulating ion and proton currents and maintaining the cristate are discussed in some details.

I. INTRODUCTION

Mitochondria are cellular organelles found in most eukaryotic cells. One of the essential roles of mitochondria is to generate cellular energy in the form of adenosine triphosphate (ATP) through oxidative phosphorylation [1, 2]. They are also responsible for various fundamental cellular functions, including calcium signaling, apoptosis, maintenance of reactive oxygen species (ROS), and metabolic regulation [3, 4]. To perform these functions properly, mitochondria frequently undergo dynamic shape changes during the mitochondrial fission and fusion events, such as separating or merging [5]. Mitochondria are also responsive to mechanical stimuli by changing their shapes and functions. For example, it has been observed that the elongation of mitochondria under mechanical strain can result in the release of excess cytochrome *c* [6, 7]. The increase in cytochrome *c* causes a decline of mitochondria membrane potential and increases the ROS production [8, 9] which in turn, trigger apoptosis and cell death. Furthermore, mitochondria also undergo deformation which happens, for examples, within narrow axonal spaces in neurons to avoid clashing and entangling with each other [10, 11], during the cell migration through narrow microfabricated channels [12], during the cardiac mechanical cycle [13], or exposure to osmotic pressure [14]. Moreover, the inner mitochondrial

is highly folded to form curved structures called cristae to increase the capacity of the mitochondrion to synthesize ATP. All these features indicate that mechanical properties of mitochondria are essential for their function and survival [5–7].

The experimental study of mitochondrial mechanics is very challenging. To date, only limited methods are available to mechanically perturb mitochondria for studying their mechanical properties [7, 15–17]. The atomic force microscopy (AFM) technique has been used to apply pressure to deform mitochondria, allowing the study of the mechanical force-induced mitochondrial fission [7]. A micropipette aspiration assay was used to study the effects of osmotic pressure or pH on the deformability of the mitochondrial membrane [15, 18]. Another method involves using motile bacteria to move throughout the host cells to collide and deform mitochondria, but this method is uncontrollable and unpredictable [7]. Song et al. have proposed an optogenetic approach to deform mitochondria via light-induced recruitment of molecular motors onto mitochondria [16]. Recently, Komaragiri et al. developed a microfluidic technology capable of determining the mechanical properties of individual mitochondria. This method has been applied to study the mechanism by which mitochondria respond to the presence of oxidative stress [17].

From the theoretical side, several mathematical models and continuum mechanic simulations have been developed to study mitochondrial mechanics [14, 17, 19–26]. Urchin developed an elastic-mathematical theory to calculate the Young's modulus and stresses of cells and

* Corresponding author: nguyen@ibpc.fr

mitochondria during the swelling process [19]. Theoretical models based on the Euler-Lagrange equation have been developed to describe the mechanical properties, including bending and stretching of cell and mitochondrial membranes [20–26]. Various kinetic models for simulation and prediction of in-vivo mitochondrial swelling have been proposed, which contribute to our understanding of the mechanisms of metabolic and functional changes in the cell under physiological and pathological conditions [14]. Hydrodynamic simulations using the finite element method have also been performed to estimate the mechanical properties of suspended mitochondria [17]. Finally, several molecular dynamics (MD) simulations have been carried out to study various aspects of mitochondria [27–30]. For example, Skulj et al. carried out an MD simulation of the elusive matrix-open state of the mitochondrial ADP/ATP carrier [27]. Atomistic simulations have been used to study the effects of charged lipids on mitochondrial outer membrane dynamics, showing that the overall effect of the accurate lipid composition on the water-membrane interface should not be ignored [28]. Wilson et al. studied the cardiolipin-dependence properties of mitochondrial membranes by atomistic MD simulations, showing that changes in cardiolipin concentration result in minor changes in the structural properties of the membranes, but the lipid diffusion is significantly affected [29]. Recently, Pezeshkian et al. carried out large-scale coarse-grained MD simulations of an entire mitochondrion with a realistic size and shape, opening the way to whole-cell simulations at the molecular level [30].

The use of a continuum membrane model can provide valuable insights into general membrane bending and deformation behaviour. However, they do not capture the molecular-level interactions and structural features of lipids, therefore these models might not account for complex phenomena, such as lipid phase transitions, lateral phase separation, or the formation of lipid domains, which can have a significant impact on membrane elasticity. To study the elasticity of mitochondrial membranes comprehensively, especially when considering the influence of lipid composition and molecular details, the molecular dynamics simulation approach may be more appropriate. However, to the best of our knowledge, no molecular dynamics simulations have been specifically aimed at studying the elasticity of mitochondrial membranes. This serves as our primary motivation for launching a molecular dynamics simulation study of various mitochondrial membrane models, encompassing both inner and outer mitochondrial membranes. For this purpose, we construct three atomistic computational models of the inner mitochondrial membrane (IMM) and three of the outer mitochondrial membrane (OMM) models based on previous theoretical and experimental data [29–32]. For each membrane model, a long all-atom simulation of 2 microseconds is carried out to ensure adequate sampling. This is crucial because it has been demonstrated that the formation of lipid clusters has a significant impact on the

elasticity of mitochondrial membranes. Given that lipid cluster formation is a slow process, conducting lengthy simulations becomes essential to verify the cluster formation. The MD simulations enable us to calculate various structural quantities and elastic moduli of the membrane models. Our findings allow us to examine the effects of specific lipids, such as cardiolipin and cholesterol, as well as the impact of symmetry/asymmetry on the structure and elasticity of the OMM and IMM models.

II. METHODOLOGY

A. Mitochondrial membrane models

The IMM and OMM contain a variety of phospholipids such as phosphatidylcholine (PC), phosphatidylethanolamine (PE), phosphatidylserine (PS), phosphatidylinositol (PI), cardiolipin (CL) and cholesterol [31]. It has been shown that the concentration of CL is higher in IMM, $\sim 5 - 20\%$, and lower in OMM, $\sim 0 - 2\%$ [33–38]. Currently, there are no accurate in-silico mitochondrial membrane models that take into account all lipid compositions. Most of MD simulation studies have been conducted using models with 2-4 lipid components. In this work, we will not develop new models, but instead, employ various models developed from previous work [29, 30], and focus on their structural property and elasticity.

The first two OMM models, called O1 and O2, consist of three lipid components including: 1-palmitoyl-2-oleoyl-sn-glycero-3-phosphocholine (POPC), 1,2-dioleoyl-sn-glycero-3-phosphoethanolamine (DOPE), and 1,3-Bis-[1,2-di-(9,12-octadecadienoyl)-sn-glycero-3-phospho]-sn-glycero (CL) lipids. The concentration of CL is 0 % in O1 and 2 % in O2, and the lipid ratio POPC:DOPE=2:1 is the same for both models. The third OMM model, O3, contains POPC, 1-stearoyl-2-arachidonoyl-sn-glycero-3-phosphoinositol (SAPI), 1-stearoyl-2-arachidonoyl-sn-glycero-3-phosphoethanolamine (SAPE) lipids and cholesterol (CHL) with the lipid ratios (POPC:SAPE:SAPI:CHL)=(55:20:20:5) for the inner leaflet, and (POPC:SAPE:SAPI:CHL)=(50:40:0:5) for the outer leaflet [30].

The first two IMM models, I1 and I2, have the same DOPE and POPC lipid compositions as the O1 and O2, but the CL concentration is 7 % in I1, and 15 % in I2. The third IMM model, called I3, consisting of POPC, CL, 1-palmitoyl-2-oleoyl-sn-glycero-3-phosphoethanolamine (POPE), and SAPI lipids. The lipid ratios are (POPC:POPE:SAPI:CL)=(30:30:10:30) for the inner leaflet, and (POPC:POPE:SAPI:CL)=(50:40:0:10) for the outer leaflet [30]. We should note that the lipid compositions of the O3 and I3 models are taken from experiments [31, 32]. The O1, O2, I1, and I2 models allow us to study the differences in the structure and elasticity of the inner and outer membranes due to the

differences in their CL concentrations. Each membrane model consists of 600 lipids. The details of lipid compositions of all mitochondrial membrane models are listed in Table I.

Model	Leaflet	DOPE	POPC	POPE	SAPE	SAPI	CL	CHL
O1	Outer	101	199	0	0	0	0	0
	Inner	101	199	0	0	0	0	0
O2	Outer	98	196	0	0	0	6	0
	Inner	98	196	0	0	0	6	0
O3	Outer	0	165	0	120	0	0	15
	Inner	0	165	0	60	60	0	15
I1	Outer	93	186	0	0	0	21	0
	Inner	93	186	0	0	0	21	0
I2	Outer	85	170	0	0	0	45	0
	Inner	85	170	0	0	0	45	0
I3	Outer	0	150	120	0	0	30	0
	Inner	0	90	90	0	30	90	0

Table I. The total number of each lipid type in the outer and inner leaflets of the outer mitochondrial membrane O1, O2, O3 models, and the inner mitochondrial membrane I1, I2, and I3 models.

B. Molecular dynamics simulations

Given the numbers of lipids listed in Tab.I, we use the Membrane Builder in CHARMM-GUI platform [39] to build the membranes. The all-atom CHARMM36 force field [40] and the TIP3P water model are used to model the lipids and solvent, respectively. The side-view and top-view of the built membranes are shown in Fig.1. The initial dimensions of the primary cell are $(L_x, L_y, L_z) = (14, 14, 8)$ nm, containing around 80000 membrane atoms, 138000 water atoms. Sodium cations and chloride anions are added to neutralize the systems. Starting from each initial structure, an equilibrium MD simulation is carried out for 100 ns, followed by a production run for 2000 ns in the NPT ensemble with the pressure $P = 1$ bar and temperature $T = 303$ K. The GROMACS simulation package [41] is used for the simulation. The semi-isotropic Parrinello-Rahman barostat [42] and the Nose-Hoover thermostat [43, 44] are used to maintain the pressure and temperature of the system at the desired values. The equations of motion are integrated using the leapfrog algorithm with a time step of 2 fs. The electrostatic interactions are calculated using the particle mesh Ewald method and a cutoff of 1.2 nm [45]. The van der Waals interaction used force switched to zero from 1.0 to 1.2 nm. The nonbonded pair lists are updated every 5 fs. The data is saved for every 50 ps for subsequent analyses.

C. Data analysis

1. The area per lipid

The area per lipid (A_L) was estimated by calculating the projection of the average area per lipid phosphate head group on the xy -plane of the membrane. In this study, we applied the GridMAT-MD program [46] to compute the A_L . The detail of algorithm is described in the work of W. J. Allen et al [46].

2. The acyl chain order parameter

The order parameter is defined as a measure of the orientation mobility of the C-H bond:

$$S_{CD} = \frac{1}{2} \langle 3\cos^2\theta - 1 \rangle, \quad (1)$$

where θ is the angle between the bilayer normal z -axis and a C-H bond vector along an acyl tail of a lipid. The brackets $\langle \dots \rangle$ represent the temporal and molecular ensemble averages [47].

3. The membrane dipole potential

The dipole potential profile $\psi(z)$ of a membrane is calculated from the charge density $\rho(z)$ via Poisson's equation:

$$\frac{d^2\psi(z)}{dz^2} = -\frac{\rho(z)}{\epsilon_0}, \quad (2)$$

where ϵ_0 is the permittivity constant. The periodic boundary condition used in the simulation implies that: $\psi(0) = \psi(L_z)$. By choosing $\psi(0) = 0$, the dipole potential of the membrane is calculated as [48]:

$$\psi(z) = -\frac{1}{\epsilon_0} \int_0^z (z-t)\rho(t)dt + \frac{z}{\epsilon_0 L} \int_0^L (L-t)\rho(t)dt. \quad (3)$$

Analytical steps connecting Eqs. 2 to 3 is provided in Supplementary Information. In our work, the simulation box was divided into 500 slabs (0.016 nm) along the z -direction, and the charge density $\rho(z)$ can be calculated by counting the number of charges in each slab.

4. Elastic modulus

The elastic moduli of mitochondrial membranes are estimated by employing the method of Levine et al. [49–51]. It is useful to summarise the main aspects of the method here. The orientation of each lipid molecule is described by a unit vector n^α with $\alpha = 1$ and 2 denoting the lipids belonging to the outer and inner leaflets, respectively. For the POPC, POPE, DOPE, SAPI and SAPE

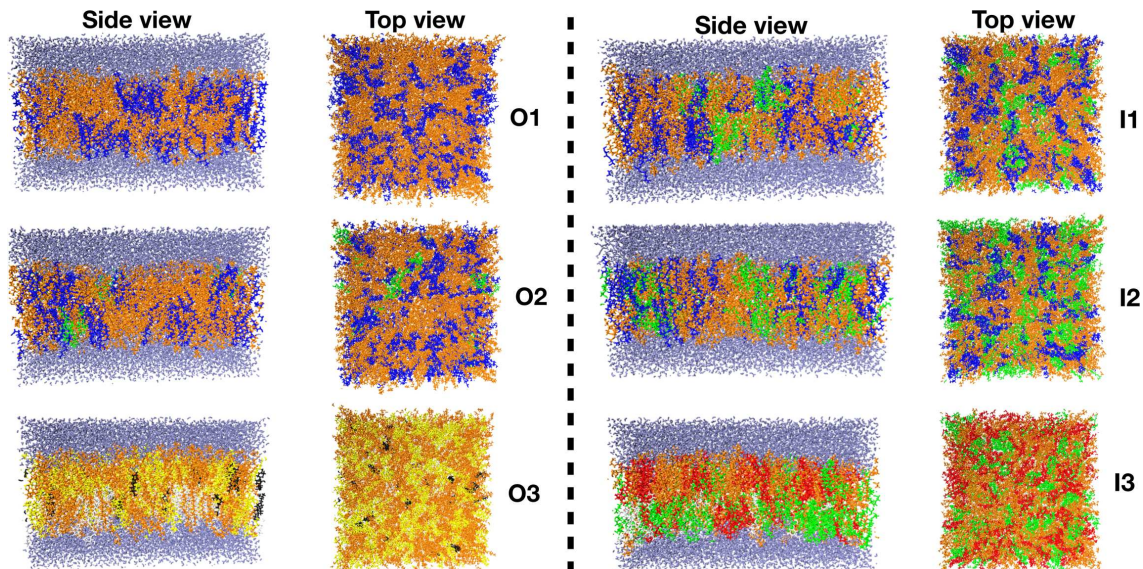


Figure 1. The initial structure of the OMM (left panels) and IMM (right panels) models built by CHARMM-GUI. Color coding is DOPE (blue), POPC (orange), CL (green), POPE (red), and SAPI (white), SAPE (yellow) and cholesterol (black). Water molecules are shown in ice-blue.

lipids \mathbf{n}^α points from the midpoint between the phosphorus (P) and glycerol (C2) atoms of the head group to the midpoint between the two terminal methyl carbons of the two lipid tails. Each CL lipid has four acyl tails, thus we assign two unit vectors to each CL lipid. The first unit vector points from the midpoint between the phosphate atom P1 and glycerol C32 to the midpoint between the two terminal methyl carbons of two lipid tails sn-1 and sn-2. The second unit vector points from the midpoint between the phosphate atom P3 and glycerol C18 to the midpoint between the two terminal methyl carbons of two lipid tails sn-3 and sn-4. For each cholesterol molecule, the unit vector directs from C3 to C17 atoms. The unit vector of a representative lipid DOPE and a CL is shown in Fig. 2. The vectors of the other lipids are shown in Fig. S2. The projection of

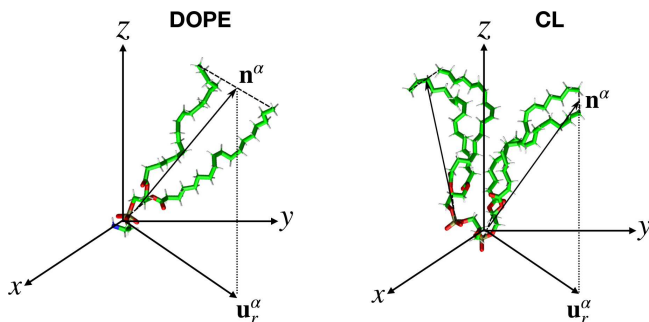


Figure 2. Molecular structure of CL and DOPE lipids used to construct the membranes in this study. The orientation of DOPE lipid is described by a unit vector \mathbf{n}^α , while two unit vectors are needed for a CL molecule. The projection of the orientation vector on the xy plane of the membrane is denoted as \mathbf{u}_r^α .

\mathbf{n}^α on the xy plane of the membrane is denoted as $\mathbf{u}_r^\alpha(\mathbf{r})$, ($\mathbf{r} = \mathbf{r}(x, y)$). Let $\mathbf{u}_q^\alpha(\mathbf{q})$ be the Fourier transformed of $\mathbf{u}_r^\alpha(\mathbf{r})$. The orientation vector of the bilayer is then defined as $\mathbf{u}_q(\mathbf{q}) = [\mathbf{u}_q^1(\mathbf{q}) - \mathbf{u}_q^2(\mathbf{q})]/2$, whose longitudinal component is $u_q^\parallel = 1/q[\mathbf{q} \cdot \mathbf{u}_q]$ and transverse component is $u_q^\perp = 1/q[\mathbf{q} \times \mathbf{u}_q] \cdot \hat{z}$. It has been shown that [49–51]

$$\langle |u_q^\parallel|^2 \rangle = \frac{k_B T}{K_c q^2}, \quad \langle |u_q^\perp|^2 \rangle = \frac{k_B T}{K_\theta + K_{tw} q^2}, \quad (4)$$

where T is temperature, k_B is Boltzmann's constant, K_c , K_θ and K_{tw} are the bilayer bending, lipid tilt and twist moduli, respectively. The angular bracket $\langle \dots \rangle$ denotes a time and ensemble average over all lipid and cholesterol molecules, which is directly obtained from the MD trajectory. We have implemented this method and used it to calculate elastic moduli of healthy membrane, cancer membranes [52] and Alzheimer's disease membranes[53].

5. Membrane curvature

The curvature of the membrane can be described by the free-energy derivative of each leaflet at the planar curvature. It can be calculated from the pressure along the membrane normal, $p(z) = p_L(z) - p_N(z)$, where $p_L(z)$ and $p_N(z)$ are the lateral and normal components of the pressure tensor, respectively. We used the local stress tensor method developed by Arroyo and colleagues [54–56] to calculate the pressure tensor. The method was implemented in the GROMACS simulation package and named as GROMACS-LS. The covariant central force decomposition CCFD method [56] is used to decompose multi-body potential forces. The leaflet free energy

derivative at planar curvature can be defined by the first moment of the pressure profile [57, 58]:

$$\bar{F}'(0) = \left. \frac{d\bar{F}}{dR^{-1}} \right|_{R^{-1}=0} = - \int_{-\infty}^{\infty} dz zp(z) \quad (5)$$

where the bar means that the free energy is expressed per unit lipid area. Nonvanishing $\bar{F}'(0)$ implies that the membrane is not energetically stable, so it would bend toward a preferred curvature.

III. RESULTS

In the following, we present the structural and elastic properties of three OMM models (O1, O2, and O3) and three IMM models (I1, I2, and I3). All results are obtained using 2000 ns trajectories. The error bars are calculated by using the block average method with five time blocks, each consisting of 400 ns.

A. Area per lipid

Model	A_L (\AA^2)		d (\AA)
	Outer	Inner	
O1	62.16 ± 0.08	62.17 ± 0.08	40.42 ± 0.29
O2	62.20 ± 0.13	62.20 ± 0.13	40.43 ± 0.29
O3	60.12 ± 0.07	60.12 ± 0.07	40.92 ± 0.30
I1	62.51 ± 0.06	62.51 ± 0.06	40.27 ± 0.25
I2	63.33 ± 0.08	63.33 ± 0.08	39.97 ± 0.27
I3	63.17 ± 0.08	63.17 ± 0.08	40.19 ± 0.26

Table II. The average area per lipid phosphate head group (A_L) of the outer and inner leaflets, and the thickness (d) of six mitochondrial membrane models. The error bars are obtained by utilizing the block averaging method with 5 blocks, each consisting of 400 ns.

To understand the lipid packing in membranes, we calculate the area per phosphate head group of a lipid, A_L , which is the average area occupied by individual phosphate head groups in the membrane. The average results of the inner and outer leaflets of each membrane model are listed in Tab.II. The time evolution of A_L is shown in Fig.S3 for all membrane models. As expected for symmetric membranes, the A_L value for the OMM models O1 and O2 is similar between the outer and inner leaflets. The A_L value remains almost unchanged, at $\sim 62 \text{ \AA}^2$, with increasing CL concentrations from 0% (O1) to 2% (O2). For the OMM O3 model, the lipid compositions in the inner and outer leaflets are different (120 SAPE lipids in the outer leaflet, and 60 SAPE, 60 SAPI lipids in the inner leaflet), but the total number of lipids in both leaflets is the same, thus there is no major difference in A_L in both leaflets. The lipids in O3 are more packed, with $A_L \sim 60 \text{ \AA}^2$ compared to O1 and O2 with $A_L \sim 62 \text{ \AA}^2$. This is partly due to the presence of

5% cholesterol in O3 which is absent in O1 and O2. At such low concentrations, cholesterol can insert itself between the fatty acid tails of the phospholipid molecules in the membrane, increasing the lipid packing.

For the IMM models, the value of A_L is the same between the outer and inner leaflets for I1, I2, and I3. The value of A_L slightly increases with increasing CL concentration from 7% in I1 to 15% in I2, which is consistent with the results of Wilson et al.[29]. Surprisingly, although the lipid composition of I3 differs significantly from that of I1 and I2, all A_L values are very similar. Compared to the O1 and O2 models, the presence of 7% CL in I1 does not result in changes in lipid packing, and the presence of 15% CL only slightly increases A_L by approximately 2% compared to 0% CL in O1.

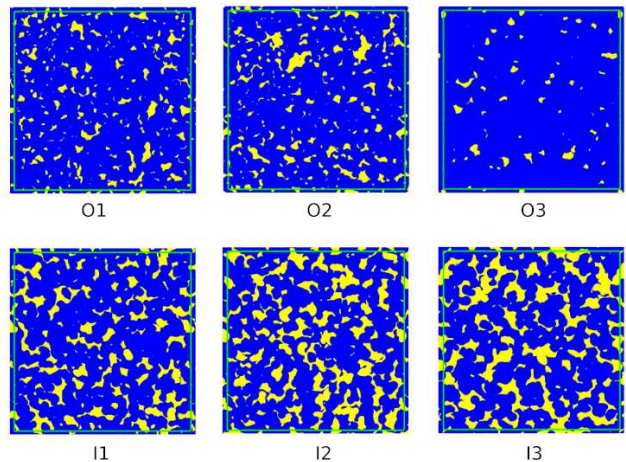


Figure 3. Lipid packing defects (yellow) for the OMM membrane models O1, O2, O3, and IMM membrane models I1, I2, I3. The green box indicates the periodic boundary condition cell. Shown are results of the snapshot at 2000 ns for each system.

To investigate finer packing differences, we assessed the lipid packing defects in all membrane models. This analysis is especially valuable for discerning the effects induced by conical lipids, such as CL. The packing defects were quantified using a recently developed method by Wildermuth et al. [59], which identifies areas on the lipid membrane surface where the topmost atom is nonpolar. As an example, the resulting defect maps of the snapshot at 2000 ns, depicted in Fig. 3 for OMM and IMM models, indicate the polar region (blue color) comprising all atoms in the lipid head groups and atoms up to the carbon below the carbonyl group, while the nonpolar region (yellow color) includes all atoms below the second carbon in the lipid tail. Our observations reveal that both the size and the number of individual defects (yellow color) on the membranes increase with rising CL concentration, ranging from 0% (O1) to 15% (I2). To explain this, we note that the CL molecule consists of two phosphatidic acids linked together by a short glycerol bridge, resulting in a conical shape with a larger cross-sectional area in the nonpolar tail relative to the polar head [see Fig. 2]. Con-

sequently, the extended tails of CL lipids exert a repulsive force on neighboring lipids, leading to the formation of empty areas (defects) on the membrane surface around smaller head groups. As a consequence, a higher concentration of CL correlates with an increased occurrence of defects. The I3 membrane, with a high CL concentration, exhibits larger defects. On the other hand, the O3 membrane is less defected because it lacks CL lipids and contains cholesterol, which increases lipid packing. We also calculate the membrane defect ratio, which is defined as the fraction of the total defect area with respect to the total membrane area, and the results averaged over the last 100 ns are (0.09, 0.10, 0.03) for (O1, O2, O3) membranes, and (0.17, 0.22, 0.24) for (I1, I2, I3) membranes [Fig. S5]. It should be noted that a nearly invariant area per lipid [Tab. II] coexists with large differences in packing defects [Fig. 3]. This discrepancy could arise because, by definition, the area per lipid is a global metric, while the defect ratio is a local metric.

Overall, our results demonstrate that the average lipid packing is not significantly influenced by the concentration of CL. However, there is a notable increase in local lipid packing defects with rising CL concentration. The presence of cholesterol enhances lipid packing and consequently reduces the occurrence of packing defects.

B. Electron density and membrane thickness

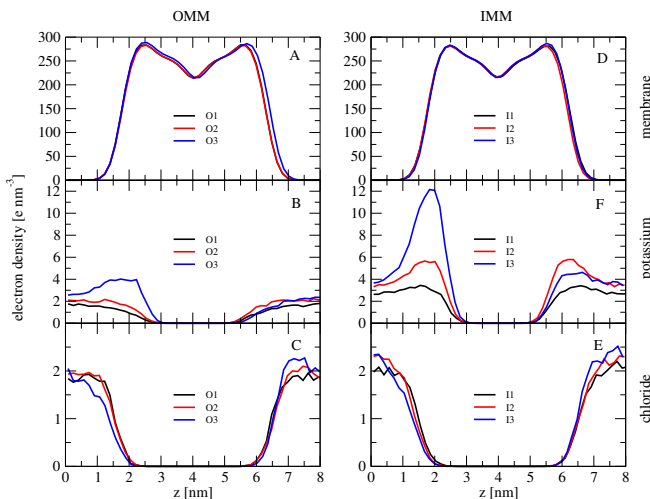


Figure 4. Electron density of the lipid membrane, the potassium ions, and the chloride ions along the z direction of all mitochondrial models.

Next, we investigate the structure of the membranes by analyzing their charge distribution and thickness. To this end, we calculate the electron density profiles of the membranes, potassium ions, and chloride ions in all the considered models along the z -direction. The results are shown in Fig. 4. Overall, the electron density profiles of

all OMM models [Fig. 4(A)] and IMM models [Fig. 4(D)] are very similar and display four major features of different molecular components, including the terminal methyl group of lipid tails ($z \sim 4.0$ nm), the methylene chains ($z \sim 3.5$ nm and 4.5 nm), the phospholipid head groups ($z \sim 2.5$ nm and 5.5 nm), and the zwitterionic groups ($z \sim 1.0$ nm and 7.0 nm). This suggests that the differences in lipid compositions have a minimal impact on the electron density profiles of the membranes. We should mention that the calculated peak electron densities for the phospholipid head groups of all membranes (water is not included) are approximately 300 electrons/ nm^3 , which is in qualitative agreement with previous MD simulation studies using different all-atom force fields [60, 61], coarse-grained force field [62], and X-ray scattering experiments [63, 64]. The membrane thickness, which is defined as the distance between two peaks located at the phospholipid head groups of the electron density profile, is approximately 4.0 nm for all models [see Tab. II].

Looking at the electron density profiles of the positively charged potassium ions in the OMM models O1, O2 [Fig. 4(B)] and the IMM models I1, I2 [Fig. 4(E)], we observe that the peaks near the position of the phosphate head groups ($z \sim 2.5$ nm and 5.5 nm) of the membranes increase with increasing CL concentration. For instance, the highest peak of profile is 5.7 e nm^{-3} in the I2 (15% CL) model, but only 2 e nm^{-3} in the O2 (2% CL) model. This is because each CL lipid has two negatively charged phosphate groups, so an increase in CL concentration results in a more negatively charged membrane surface, which promotes the binding of positively charged ions.

Due to the asymmetric lipid compositions of the inner and outer leaflets, the potassium density in the O3 and I3 membranes exhibits an asymmetrical profile, with high density on the inner leaflet side and low density on the outer leaflet side. This is because the inner leaflet of O3 contains the SAPI lipids, which are absent in the outer leaflet, and the inner leaflet of I3 contains more negatively charged phosphate groups, which come from CL (90 CL lipids) than the outer leaflet (30 CL lipids).

The density profiles of the negatively charged choline ions are similar for the OMM and IMM models [Figs. 4(C), (F)]. This is because each CL lipid, like the DOPE and POPC lipids, has only one positively charged zwitterionic head group, therefore an increase in CL concentration in O1 and O2 or I1 and I2 compensates for the decrease in DOPE and POPC concentrations, resulting in slight difference in the positively charged membrane surface and the binding of negatively charged ions. Similarly, each SAPI has a positively charged inositol group, and each SAPE lipid has a positively charged ethanolamine group, thus although the lipid compositions in O3 or I3 are different from those in O1, O2 or I1, I2, the total number of the positively charged groups on the membrane surface is similar, resulting in similar binding affinity of the negatively charged chloride ions.

Overall, our findings indicate that the membrane electron density profile of the OMM (O1, O2, O3) and IMM

(I1, I2, I6) are quite similar, but the potassium ion profile is higher in the INM models than in the OMM models, and this is mainly due to the contribution of the CL lipid. The chloride ion profile does not vary much between the IMM and OMM models.

C. Acyl chain order parameter

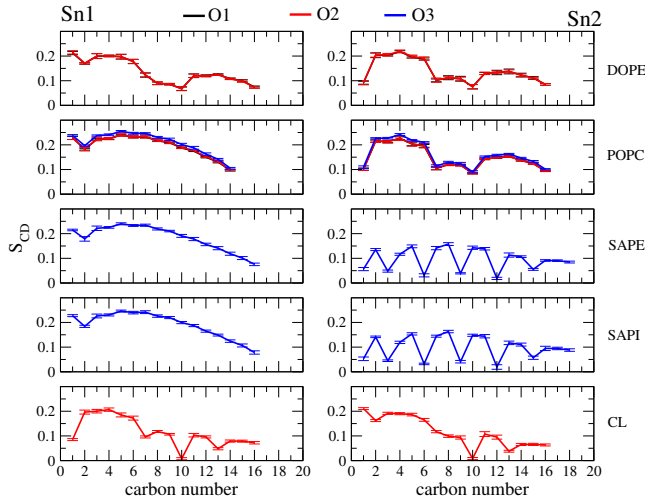


Figure 5. The order parameters of two tails sn-1 (left panels) and sn-2 (right panels) of five lipid types DOPE, POPC, SAPE, SAPI and CL of the O1 (black), O2 (red) and O3 (blue) membranes. Carbon atom numbers increase in the direction of the tail termini. Shown are results averaged over snapshots of the 2000 ns trajectories. The error bars are obtained by utilizing the block averaging method with 5 blocks, each consisting of 400 ns.

To investigate the influence of lipid composition on the flexibility of carbon tails, we calculate the order parameters for carbon atoms of the acyl chain tails of each lipid type using Eq.1. There are 17 order parameters in all tails of DOPE and CL lipids. For POPC and POPE, there are 15 order parameters in tail sn-1 and 17 in tail sn-2. For SAPI and SAPE lipids, there are 17 order parameters in tail sn-1 and 19 in tail sn-2. However, it is not possible to compute the order parameter for the first carbon atom as it lacks neighbouring atoms from which the local molecular axis is computed. Fig.5 displays the order parameters for all lipid types in the OMM models. As observed, the DOPE lipids in O1 and O2 exhibit very similar ordering in both tails sn-1 and sn-2, indicating that the addition of 2% of CL in O2 does not affect the ordering of the main lipid component, DOPE. The POPE lipids are more ordered in O3 than in O2, presumably because the presence of cholesterol in O3 enhances the ordering of lipids. The order parameters of the SAPE and SAPI lipids in O3 are very similar. It is worth mentioning that the SAPI and SAPE lipids consist of a stearyl

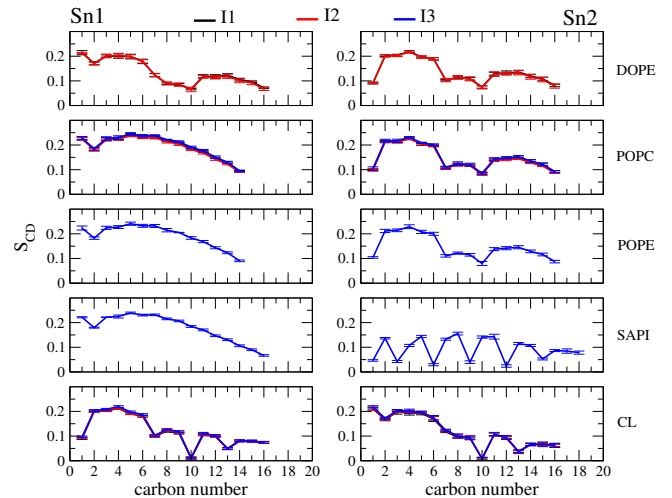


Figure 6. The order parameters of two tails sn-1 (left panels) and sn-2 (right panels) of five lipid types DOPE, POPC, POPE, SAPI and CL of the I1 (black), I2 (red) and I3 (blue) membranes. Carbon atom numbers increase in the direction of the tail termini. Shown are results averaged over snapshots of the 2000 ns trajectories. The error bars are obtained by utilizing the block averaging method with 5 blocks, each consisting of 400 ns.

tail (sn-1) with no double bonds (saturated fatty acid) and an arachidonoyl tail (sn-2) with four double bonds (polyunsaturated fatty acid). As a consequence, the order parameters of the sn-1 tail do not show kinks, similar to the sn-1 tail of the POPE lipid. In contrast, the sn-2 tail exhibits four kinks, which disrupt the regular packing of the acyl chains in the lipid bilayer, leading to a less ordered and more fluid-like region around the double bonds. The CL lipid has four acyl chains attached to the positions 1 and 3 of the glycerol backbone. For simplicity, the order parameters of the sn-1 or sn-2 tail shown in Fig. 5 are actually averaged over the two sn-1 or sn-2 tails. As each tail has two double bonds, located at the 11th and 14th carbon-carbon positions, the order parameters are low at these positions.

Fig.6 displays the order parameters for all lipid types in the IMM models. The order parameters of the DOPE lipid or POPC lipid are very similar between I1, I2, O1, and O2 [Fig.5]. This suggests that the increase of the CL lipid concentration up to 15% (I2) still does not significantly affect the ordering of DOPE or POPC lipids in these membranes. The POPE lipid is only present in the I3 membrane, and its behaviour is quite similar to that of the DOPE lipid. The ordering of the SAPI and CL lipids in the IMM membrane is not significantly different from those in the OMM membranes.

Finally, we note that the POPC lipid is slightly more ordered than the DOPE and POPE lipids in all models. This is because POPC has a saturated fatty acid tail, which makes it more rigid, and a choline head group,

which can interact strongly with water molecules. Comparing the DOPE with the POPE lipids, we observe that DOPE lipid in OMM models (O1 or O2) or in IMM models (I1 or I2) is slightly less ordered than the POPE lipid in I3 model. This is because DOPE has two unsaturated fatty acid tails, which introduce kinks into the membrane structure and prevent tight packing of the lipid molecules. In contrast, POPE has a saturated fatty acid tail, which makes it more rigid and ordered. The SAPI and SAPE lipids in the O3 or I3 are less ordered than the DOPE, POPC and POPE due to their highly unsaturated arachidonoyl chains that disrupt the tight packing of the tails and reduce their order.

Overall, the order of each lipid type is not significantly different between membranes, whether it is the OMM or IMM models. This indicates that an increase in the CL concentration in the IMM does not enhance the order of lipids. Furthermore, the presence of cholesterol, SAPI, and SAPE lipids also does not cause significant changes in membrane ordering.

D. Membrane dipole potential

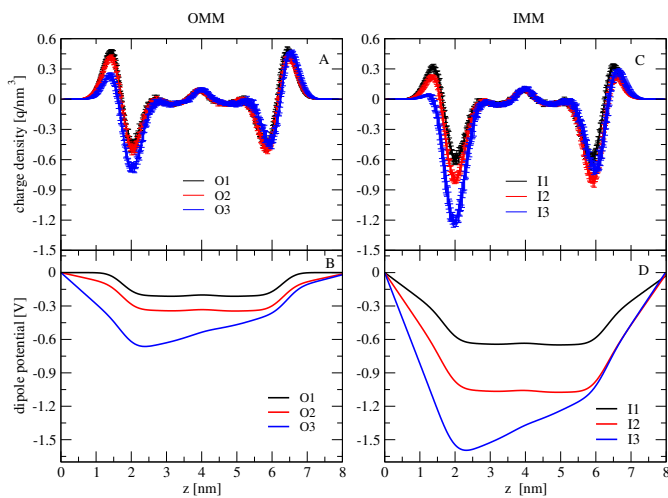


Figure 7. Charge density (upper panels) and dipole potential (lower panels) along z -direction of all mitochondrial models. The error bars in the charge density are obtained by utilizing the block averaging method with 5 blocks, each consisting of 400 ns.

The charge density profiles of the OMM models O1, O2, and O3 are shown in Fig.7(A). Overall, the profiles exhibit three main peaks contributed by different charge components, including the positively charged terminal methyl groups in the lipid tails ($z \sim 4.0$ nm), the negatively charged phosphate groups ($z \sim 2$ nm and 6 nm), and the positively zwitterionic groups ($z \sim 1$ nm and 6.5 nm). Because each CL lipid has two negatively charged phosphate groups, an increase of 2% of CL in O2

slightly increases its negative peak compared to O1. In contrast, due to the reduced number of DOPE and POPC lipids in O2 [Tab.I], its positive peak contributed by the zwitterionic groups is lower than in O1. The O3 model exhibits an asymmetric charge density profile. The positive peak in the outer leaflet ($z \sim 6.5$ nm) is higher than that in the inner leaflet ($z \sim 1.5$ nm) because the outer leaflet contains a larger number of SAPE lipids compared to the inner leaflet. In contrast, the negative peak in the inner leaflet ($z \sim 2$ nm), contributed by POPC, SAPE and SAPI lipids, is higher than that in the outer leaflet ($z \sim 6$ nm), which is contributed by only POPC and SAPE lipids. The dipole potentials of O1, O2, and O3 are calculated from their charge densities and shown in Fig.7(B). As seen, the increase in negatively charged profiles from O1 to O2 and O3 results in a more negative dipole potential, with a potential depth of ~ -0.2 V for O1, -0.3 V for O2 and -0.7 V for O3. We note that these values are in the experimental estimation range of -0.2 to -1 V [65]. Again, the dipole potential of O1 and O2 are symmetric while the potential of O3 is asymmetric.

For the IMM models I1 and I2, the charge density profiles behave similarly to those of the OMM models, but with stronger negative peaks at $z \sim 2$ nm and 6 nm and weaker positive peaks at $z \sim 1.5$ nm and 6.5 nm as shown in Fig.7(C). This is because of the decreased DOPE and POPC concentrations, which leads to the reduction of positively charged zwitterionic groups (see Tab. I), and the increased CL concentration that raises the number of negatively charged phosphate groups. The IMM model I3 shows an asymmetric charged profile with a very deep negatively charged peak at $z \sim 2$ nm in the inner leaflet, which is primarily contributed by the negatively charged phosphate groups of POPC, POPE, CL and SAPI lipids. In contrast, the lower negatively charged peak at $z \sim 6$ nm in the outer leaflet is due to the smaller number of CL and the absence of SAPI lipids in this leaflet. Consequently, the dipole potentials of the I1, I2, and I3 membranes are more negative than those of the OMM models O1, O2, and O3, with the potential depth of ~ -0.6 V for I1, -1.0 V for I2, and -1.6 V for I3.

Overall, our results indicate that the dipole potential of the mitochondrial membranes increases as the concentration of CL rises. This shows that, the IMM exhibits a more negative dipole potential than the OMM.

E. Membrane elastic properties

From the simulation trajectory, we calculate the orientation vectors \mathbf{u}_i^α , [Fig.2], of all lipid and cholesterol molecules. The power spectra as a function of the wavelength q are calculated from Eq.4. The spectra obtained over 2000 ns are shown in Fig.8 for three OMM models. The data of the IMM models are similar, and not shown here. As seen, the spectra $\langle |u_{\mathbf{q}}^\alpha|^2 \rangle$ (weighted by q^2) are almost constant with $q < 1.5$ nm $^{-1}$ or equivalently $r > 2\pi/q \approx 4.2$ nm [Figs.8(A,B,C)]. In this plateau re-

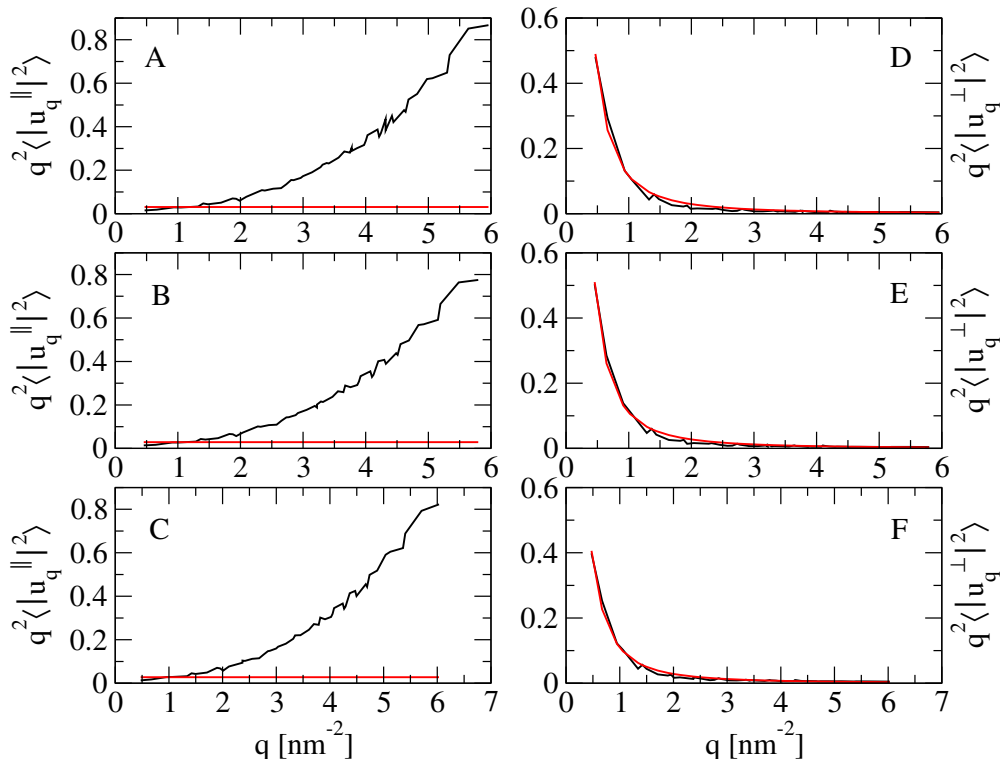


Figure 8. Power spectra of the longitudinal (weighted by q^2) (left panels) and transverse (right panels) components of the lipid orientation vectors. Shown are results of the OMM models O1 (A, D), O2 (B, E), and O3 model (C,F). The best fits of the data to Eq.4 are shown by the red lines. Only data in the range $0 < q < 1.5 \text{ nm}^{-1}$ are used for the fit of the longitudinal curves, and $0 < q < 3.5 \text{ nm}^{-1}$ for the transverse curves. The spectra are averaged over 2000 ns trajectories.

gion the theoretical prediction for K_c , Eq.4, is valid. This allows us to extract the bending constant K_c by fitting the data to a straight line [Figs.8(A,B,C)]. Note that the plateau region extends over the distances $r > 4.2 \text{ nm}$, which is much smaller than the length of the simulation box of 14 nm . Therefore, the results of K_c are well-converged with system size.

To obtain the tilt, K_θ , and twist, K_{tw} , moduli, we fit the power spectra shown in Figs.8(D,E,F) to the theoretical prediction curve, Eq.4. Here, only data within $0 < q < 3.5 \text{ nm}^{-1}$ are used for the fit. The elastic moduli of all membrane models at 303 K are listed in Tab.III.

With the presence of 2 % CL concentration in O2, the bending modulus of O2 is $14.43 \times 10^{-20} \text{ J}$, which is approximately 6% higher than that of O1 without CL. The tilt modulus, K_θ , of both models is very similar, with the difference being almost within the error bars. The twist modulus, K_{tw} , of O2 is slightly higher than that of O1. This suggests that the CL lipids tend to make the membrane stiffer. The O3 membrane has a larger bending modulus ($15.09 \times 10^{-20} \text{ J}$) and a tilt modulus ($0.21 \times 10^{-20} \text{ J}$), but a similar twist modulus compared to those of O1 and O2. To explain this, we note from Tab. I that O3 does not contain the DOPE and POPE

Model	K_c (10^{-20} J)	K_θ (10^{-20} J/nm^2)	K_{tw} (10^{-20} J)
O1	13.62 ± 0.31	0.07 ± 0.02	3.51 ± 0.12
O2	14.43 ± 0.25	0.04 ± 0.01	3.75 ± 0.18
O3	15.09 ± 0.61	0.21 ± 0.08	3.59 ± 0.11
I1	15.43 ± 0.39	0.05 ± 0.02	3.73 ± 0.31
I2	16.75 ± 0.45	0.08 ± 0.02	4.13 ± 0.14
I3	14.29 ± 0.30	0.13 ± 0.05	3.76 ± 0.12

Table III. The bending (K_c), tilt (K_θ) and twist (K_{tw}) elastic moduli of the OMM models (O1, O2, and O3) and IMM models (I1, I2, and I3). Results are calculated using Eq.4. The error bars are obtained using the block averaging method with five data blocks, each 400 ns long.

lipids, but contains only POPC with a lower number of POPC (330 lipids) than that of O1 and O2 (392 lipids), but O3 contains the SAPI and SAPE lipids as well as cholesterol (5%). It is known that the POPC lipid is generally considered to be more rigid and ordered than the POPE and DOPE lipids because POPC has a saturated fatty acid tail, which makes it more rigid, and a choline head group that can interact strongly with water molecules and other charged molecules. Therefore, the

increase in the bending modulus of O3 is likely due to the presence of cholesterol, which is well-known to affect the stiffness of lipid membranes.

For the IMM models, we observed that increasing the CL concentration from 7% (I1) to 15% (I2) leads to an increase in all three moduli: 9% in K_c , 60% in K_θ , and 11% in K_{tw} . However, even though the I3 membrane has a higher number of CL lipids (120 lipids) compared to I2 (90 CL lipids) and also contains the stiffer POPE lipid instead of the DOPE lipid in I2, the bending modulus of I3 is smaller, 14.29×10^{-20} J compared to 16.75×10^{-20} J of I2. To explain this qualitatively, we calculate the pressure profile along the membrane normal $p(z)$ (see Method) and the results are shown in Fig. 9 for the I2 and I3 models. As seen, the pressure profile of I2 is symmetric,

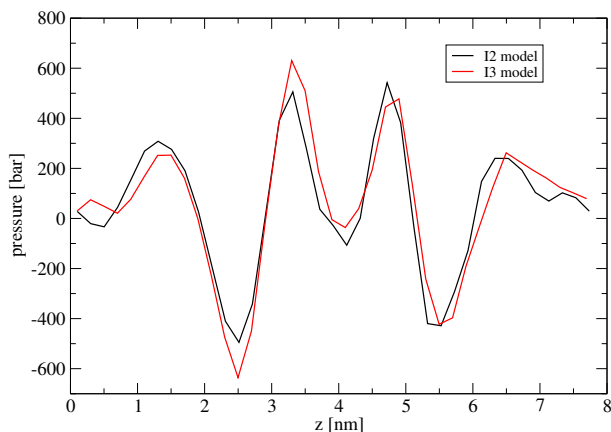


Figure 9. Pressure profile along the z direction of the IMM I2 (black) and I3 (red) models. Shown are average results obtained from the last 500 ns of trajectories.

whereas that of I3 is asymmetric, with a noticeable peak shift at $z \sim 2.5$ nm, located at the negatively charged phosphate groups. This is because the inner leaflet of I3 contains more CL than the outer leaflet, and each CL has two negatively charged phosphate groups. To characterize the membrane curvature, we calculate the free energy derivative of the I2 and I3 membranes using Eq.5 and obtain $F'(0) = -0.01$ and -0.03 kcal/mol/Å for I2 and I3, respectively. These values indicate that the I3 membrane is energetically more unstable, preferring to be bent and thus having a smaller bending modulus compared to I2.

Overall, the results indicate that CL lipids increase membrane stiffness in both OMM and IMM models. The presence of cholesterol in the OMM increases the bending and tilt moduli of the membrane. The other lipids DOPE, POPC, and POPE contribute differently to the elasticity of the membranes, depending on their concentrations.

IV. DISCUSSION

While the MD simulation technique for lipid membranes is well-established, it is important to note that the results can be influenced by the choice of computational membrane models. In real mammalian cells, the mitochondrial membranes consist mainly of phospholipids, including PC, PE, PS, CL, and cholesterol. These phospholipids are distributed asymmetrically across the lipid leaflets. Additionally, the membranes have a high protein to phospholipid ratio, with approximately 25% proteins in the OMM and 60% proteins in the IMM [66]. Our membrane models include the major lipid components PC, PE, CL, and cholesterol, but we did not include PS due to its low abundance. We considered both symmetric and asymmetric membrane models, but our models lack proteins. Nevertheless, our simulations provide insights into the effects of CL, cholesterol, and membrane asymmetry on the structure and elasticity of the membranes, which we discuss in the following.

In a previous study, Wilson et al. investigated the effect of CL concentration on the structure and dynamics of mitochondrial membranes using various membrane models consisting of PO/PE/CL lipids [29]. The authors found that changes in CL concentration had minimal effect on membrane structure but significantly impacted lipid diffusion. In our work, we use the same lipid mole fractions as the models of Wilson et al. to construct our models O1, O2, I1, and I2. We use the same CHARMM36 force field, but our simulations are longer, running for 2 μ s compared to 0.9-1 μ s simulations of Wilson et al. Our simulations also show that changes in CL concentration has minimal effect on various structural quantities such as area per lipid, membrane thickness, density profile, and lipid order parameters. This finding is consistent with previous MD simulation studies by Wilson et al. [29], Rog et al. [67], Poyry et al. [68], and experimental data of Khalifat et al. [69] for CL concentrations of up to 11%. Our simulations show that at 15% CL concentration, the lipid area increased in model I2 [Table II], which is consistent with results of Wilson et al. at the same CL concentration.

Overall, our results and previous studies suggest that over-expression of CL lipids in the IMM is not a major factor causing structural differences between the OMM and IMM, at least when the CL concentration is below 15%. We also find that membrane symmetry/asymmetry does not significantly affect membrane structure, as evidenced by the similarity in structure between our O3 and I3 models, which have a different lipid composition and asymmetry but a similar lipid packing. In a recent study, Oliveira et al. used atomistic MD simulations on five OMM membrane models composed of four lipid components (POPC, POPE, PI, and PS lipids) with different lipid ratios and showed that complex membrane compositions have relatively minor effects on membrane structural properties [28]. The area per lipid values of their models fell within the range of 61.2-62.1 Å², which is

similar to our values of 60.2-62.2 Å² [see Table II].

Taken together, all of the aforementioned results suggest that computational mitochondrial models composed of several common lipids are likely sufficient for capturing the essential structural properties of mitochondrial membranes. Several studies have investigated the

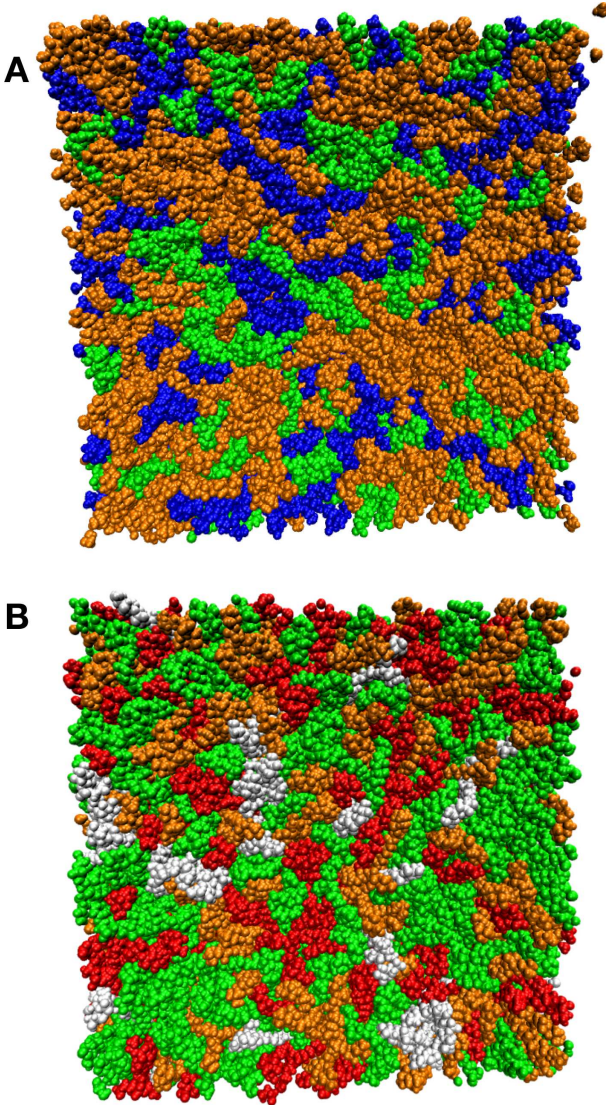


Figure 10. Snapshots from the final frame of the 2000 ns trajectory of the I2 model (A) and I3 model (B). Color coding is DOPE (blue), POPC (orange), CL (green), POPE (red), and SAPI (white)

ability of CL to induce cluster formation when mixed with other lipids because CL is primarily associated with proteins [29, 70–74]. Domenech et al. carried out experiments with membranes composed of two lipid components, CL/POPE or CL/POPC, using atomic force microscopy and showed that CL forms domains within the membrane [71, 72]. Another experimental study by Sennato et al. with membranes of CL/DPPE and

CL/DPPC (20% CL) also demonstrated domain formation [73]. However, a recent experiment by Boscia et al. showed no domain formation in membranes with a mixture of CL/DMPC (20% CL) [74]. From the theoretical side, MD simulations using MARTINI coarse-grained lipid models by Boscia et al. did not observe domain formation in CL/DMPC membranes. Atomistic MD simulations by Wilson et al. also did not observe domain formation in DOPE/POPC/CL membranes (15% CL) [29]. The authors attributed this to the simulation time being too short (0.9 - 1 μs) to observe domain formation. Our simulations, which are longer (2 μs) and use different lipid components (DOPE/POPC/CL with the I2 model and POPC/POPE/SAPI/CL with the O3 model), also do not observe domain formation. Indeed, the distribution of lipid types in the I2 and O3 membranes in the final snapshots of the 2000 ns trajectories exhibited in Fig.10 shows that lipids do not form particular domains. Moreover, we observe that CL lipids do not concentrate in specific regions. A recent experimental study by Beltran-Heredia et al. with PC/CL membranes showed that CL molecules aggregate into clusters at the curved regions of the membrane [75]. This result is consistent with the simulation results of Boyd et al., which also showed that CL locally concentrates at the curved regions of the membrane [76]. As seen from the snapshots shown in Fig.10, and from small values of the free energy derivative at planar curvature of the I2 (-0.01 kcal/mol/Å) and I3 (-0.03 kcal/mol/Å) membranes, it turns out that our membranes are rather flat and do not drive CL lipids into specific regions.

Regarding the role of CL, Wilson et al. showed that increasing the concentration of CL in membranes significantly increases the lateral diffusion of lipids [29]. In our simulations using the same models, we have uncovered a new role for CL, that is, the concentration of CL affects the dipole potential of the membrane. Specifically, the dipole potential becomes stronger with increasing CL concentration. This also implies that the IMM has a stronger dipole potential than the OMM [see Fig. 7]. While it has long been understood that the IMM has a higher dipole potential than the OMM due to its high concentration of electrochemically active components and resultant proton gradient, our research suggests that the presence of CL may also contribute to this difference. The OMM, on the other hand, is relatively permeable and lacks the concentration of electrochemically active components, leading to a lower dipole potential. Our finding suggests that CL may play a role in providing the IMM with a suitable dipole potential to tightly regulate the flux rate of protons and ions across the membrane during cellular energy production. This argument is supported by recent study showing that the transmembrane potential is critical for regulating the mitochondrial membrane proton conductance [77]. However, the full mechanism remains to be determined,

In general, our simulation results show that the mechanical properties of the OMM and IMM membranes

are different, but not significantly different. However, there are not many experimental data on the elastic moduli of mitochondrial membranes, and especially no experimental results for membranes with lipid compositions like those in our models, so it is difficult to quantify the simulation results. Recently, Schiaffarino et al. measured the bending modulus of the IMM and OMM of giant unilamellar vesicles (GUV) from porcine heart using the micropipette aspiration method and obtained $K_c = 2.32 \times 10^{-20}$ J for the IMM and $K_c = 3.23 \times 10^{-20}$ J for the OMM [18]. These values are about 4-5 times smaller than our simulation values. The difference can be attributed to three main reasons: first, the composition and ratio of lipids in OMM and IMM in the experiment are different from those in our OMM and IMM models. Second, our membranes are flat, whereas the GUVs in the experiment are curved. The curvature of the membrane can affect its bending modulus because a curved membrane has curvature stresses that help deform it, thus the bending modulus of a curved membrane is generally smaller than that of a planar counterpart. Third, there are uncertainties in both calculation and experiment. As discussed by Nagle et al. [78], values obtained in different labs and with different measuring techniques typically differ by as much as a factor of two for the same lipid at the same temperature. There are still unexplained differences in the experimental values of the bending modulus. From the simulation side, force fields are not perfect and were not aimed to represent a specific experimental systems, thus a comparison between simulation results and experimental counterparts is not straightforward. Nevertheless, both experiment and our simulation show no significant difference between OMM and IMM. Both are essentially liquid and deformable, which may be a characteristic that provides mitochondrial membranes with mechanical stability and softness adequate for easy deformation to perform functions.

Another important result from our simulation study shows that the bending modulus increases with the concentration of CL (as shown in the results of the membranes O1, O2, I1, and I3 in Table III). This result is qualitatively consistent with experimental findings that membranes containing only CL [79] or CL/PC mixed membranes [74] have a higher bending modulus than membranes containing only PC. This means that CL tends to make the membrane stiffer. However, it may seem counterintuitive that the IMM has a wrinkled shape with highly curved cristae despite containing a higher concentration of CL. From a physics perspective, a lipid membrane with a large bending modulus will be more resistant to returning to its original state when bent than a membrane with a lower bending modulus. In this context, we can see that while CL is highly concentrated in the curved regions of the IMM such as cristae [75, 76], the increase in concentration can increase the bending modulus, which can help maintain the curvature of those regions. The maintenance of the curved structure of the mitochondrial cristae is crucial for stabilizing protein

complexes necessary for respiration, oxidative phosphorylation, and ATP synthesis [80, 81].

One might assume that the IMM is stiffer than the OMM due to the high concentration of CL in the IMM compared to the low concentration in the OMM. However, the experimental study by Schiaffarino et al. on GUVs of native OMM and IMM extracts from porcine heart shows that the IMM membrane is softer than the OMM membrane [18]. Although our OMM O3 model does not contain CL, it contains 5% cholesterol, which increases the bending modulus of O3. The effect of cholesterol on membrane stiffening has been well understood. In the experiment of Schiaffarino et al., the OMM and IMM membranes contained 16.7% and 10.3% cholesterol, respectively. Therefore, the softer nature of the IMM membrane observed in the study of Schiaffarino et al. may be due to the relatively lower amount of cholesterol present in the IMM compared to the OMM. Thus, the role of CL in contributing to the increased rigidity of IMM could be similar to the role of cholesterol in contributing to the increased rigidity of OMM. Nevertheless, it is important to note that interpreting the softness/stiffness of a membrane requires careful consideration. This is because the bending energy of a membrane depends not only on the bending modulus but also on the spontaneous curvature of the membrane, as described by the Helfrich-Canham function [82, 83]: $E = K_c \int (H - H_0)^2 dA$, where K_c represents the bending modulus, H represents the local mean curvature, H_0 represents the spontaneous curvature, and dA represents the element of membrane area. As the IMM contains highly curved regions, its bending energy can still be significant, making it more deformable.

Finally, an interesting result is that the bending modulus of the I3 membrane (containing 19% CL) is smaller than that of the I1 (7% CL) and I2 (15% CL) membranes [Tab. III]. Additionally, I3 contains POPE, while I1 and I2 contain DOPE. We know that in general, a membrane containing DOPE is more fluid and softer than a membrane containing POPE. But why does I3 contain both CL and POPE, yet its K_c is still smaller than that of I1 and I2? To explain this, we note that I3 is an asymmetric membrane, with different lipid compositions in the inner and outer leaflets [Tab. I]. This asymmetry causes differences lateral pressure between the two leaflets, which creates asymmetric curvature stresses that could lead to greater membrane bending and a smaller bending modulus.

V. CONCLUSIONS

We perform MD simulations using six lipid membrane models that mimic mitochondrial membranes. The first type of model is symmetric, where the OMM and IMM models differ only in their CL concentrations. Two OMM models have 0% and 2% CL concentrations, while two IMM models have 7% and 15% CL concentrations. The

second type of model is asymmetric, where a major difference is that one OMM model contains cholesterol, and one IMM model has different CL concentrations between the inner and outer leaflets. These models allow us to investigate the effects of CL, cholesterol, and symmetric/asymmetric properties on the structure and elasticity of OMM and IMM models.

Simulation results show that membrane structure, including lipid packing, thickness, and lipid order, is nearly independent of the membrane models. This suggests that the structure of OMM and IMM is not significantly different. However, the results showed that the dipole potential of the IMM is stronger than that of the OMM due to the higher CL concentration in IMM. The strength of the dipole potential may be necessary for IMM to tightly regulate ion and proton fluxes, allowing ROS production, and function of the respiratory chain complexes. This could be one of the roles of CL, explaining why its concentration is higher in IMM than in OMM.

Our results demonstrate that an increase in CL concentration leads to an increase in the bending modulus of the IMM membrane. This is important for maintaining the curved structure, such as cristae, necessary for proper IMM function. Furthermore, while the OMM has a lower concentration of CL, it contains cholesterol, which contributes to an increase in its stiffness. As a result, the stiffness of the OMM and IMM are not significantly different.

In summary, simulation results suggest two roles of CL in IMM: regulating ion and proton fluxes by increasing the dipole potential and maintaining the curved state of cristae by increasing the bending modulus.

Supporting Information: The derivation of the dipole potential equation, the description of the orientation vectors of all lipids, the time evolution of the area per lipid, and the description of the membrane defect ratio.

Acknowledgements

This research is supported by The Grant agreement No. 101034407 of the European Union’s Horizon 2020 Research and Innovation Programme under the Marie Skłodowska Curie actions, the “Initiative d’Excellence” program from the French State (Grant “DYNAMO”, ANR- 11-LABX- 0011-01), the CNRS and the TGCC/IDRIS centers for providing computer facilities.

REFERENCES

- [1] H. M. McBride, M. Neuspiel, and S. Wasiak, “Mitochondria: More than just a powerhouse,” *Curr. Biol.* **16**, R551–R560 (2006).
- [2] G. Paradies, V. Paradies, F. M. Ruggiero, and G. Petrosillo, “Role of cardiolipin in mitochondrial function and dynamics in health and disease: Molecular and pharmacological aspects,” *Cells* **8**, 728 (2019).
- [3] D. B. Zorov, M. Juhaszova, and S. J. Sollott, “Mitochondrial reactive oxygen species (ros) and ros-induced ros release,” *Physiol. Rev.* **94**, 909–950 (2014).
- [4] W. Droge, “Free radicals in the physiological control of cell function,” *Physiol. Rev.* **82**, 47–95 (2002).
- [5] Y. J. Liu, R. L. McIntyre, G. E. Janssens, and R. H. Houtkooper, “Mitochondrial fission and fusion: A dynamic role in aging and potential target for age-related disease,” *Mech. Ageing Dev.* **186**, 111212 (2020).
- [6] S. Wu, F. Zhou, Z. Zhang, and D. Xing, “Mitochondrial oxidative stress causes mitochondrial fragmentation via differential modulation of mitochondrial fission-fusion proteins,” *FEBS J.* **278**, 941–954 (2011).
- [7] S. C. J. Helle, Q. Feng, M. J. Aebersold, L. Hirt, R. R. Gruter, A. Vahid, A. Sirianni, S. Mostowy, J. G. Snedeker, A. Saric, T. Idema, T. Zambelli, and B. Kornmann, “Mechanical force induces mitochondrial fission,” *Elife* **6**, 1–26 (2017).
- [8] K. E. Chapman, S. E. Sinclair, D. Zhuang, A. Hassid, L. P. Desai, and C. M. Waters, “Cyclic mechanical strain increases reactive oxygen species production in pulmonary epithelial cells,” *Am. J. Physiol. Lung Cell. Mol. Physiol.* **289**, L834–L841 (2005).
- [9] E. Bartolak-Suki, J. Imsirovic, Y. Nishibori, R. Krishnan, and B. Suki, “Regulation of mitochondrial structure and dynamics by the cytoskeleton and mechanical factors,” *Int. J. Mol. Sci.* **18**, 1812 (2017).
- [10] T. Misgeld and T. L. Schwarz, “Mitostasis in neurons: Maintaining mitochondria in an extended cellular architecture,” *Neuron* **96**, 651–666 (2017).
- [11] J. E. Rinholm, K. Vervaeke, M. R. Tadross, A. N. Tkachuk, B. G. Kopeck, T. A. Brown, L. H. Bergersen, and D. A. Clayton, “Movement and structure of mitochondria in oligodendrocytes and their myelin sheaths,” *Glia* **64**, 810–825 (2016).
- [12] Q. Feng, S. S. Lee, and B. Kornmann, “A toolbox for organelle mechanobiology research—current needs and challenges,” *Micromachines* **10**, 538 (2019).
- [13] E. A. Rog-Zielinska, E. T. O’Toole, A. Hoenger, and P. Kohl, “Mitochondrial deformation during the cardiac mechanical cycle,” *Anat. Rec.* **302**, 146–152 (2019).
- [14] S. Javadov, X. Chapa-Dubocq, and V. Makarov, “Different approaches to modeling analysis of mitochondrial swelling,” *Mitochondrion* **38**, 58–70 (2018).
- [15] S. Wang, C. Jiang, Y. Zhang, J. Chen, B. Wang, Q. Chen, and M. Long, “Membrane deformability and membrane tension of single isolated mitochondria,” *Cel. Mol. Bioeng.* **1**, 67–74 (2008).
- [16] Y. Song, P. Huang, X. Liu, Z. Zhao, Y. Wang, B. Cui, and L. Duan, “Light-inducible deformation of mitochondria in live cells,” *Cell Chem. Biol.* **29**, 109–119 (2019).
- [17] Y. Komaragiri, M. H. Panhwar, B. Fregin, G. Jagirdar, C. Wolke, S. Spiegler, and O. Otto, “Mechanical characterization of isolated mitochondria under conditions of oxidative stress,” *Biomicrofluidics* **16**, 064101 (2022).
- [18] O. Schiaffarino, D. V. Gonzalez, I. M. Garcia-Perez, D. A. Penalva, V. G. Almendro-Vedia, P. Natale, and I. Lopez-Montero, “Mitochondrial membrane models built from native lipid extracts: Interfacial and transport properties,” *Front. Mol. Biosci.* **23**, 910936 (2022).
- [19] S. Urchin, “Elastic-mathematical theory of cells and mitochondria in swelling process,” *Biophys. J.* **7**, 95–110 (1967).
- [20] M. Zaal, “Cell swelling by osmosis: A variational ap-

- proach,” *Interfaces and Free Boundaries* **14**, 487–520 (2012).
- [21] C. Lehrenfeld and S. Rave, “Mass conservative reduced order modeling of free boundary cell swelling problem,” *Adv. Comp. Math.* **45**, 2215–2239 (2019).
- [22] Y. Mori, “Mathematical properties of pump-leak models of cell volume control and electrolyte balance,” *J. Math. Biol.* **65**, 875–918 (2012).
- [23] H. Alimohamadi and P. Rangamani, “Modeling membrane curvature generation due to membrane–protein interactions,” *Biomolec* **8**, 120 (2018).
- [24] Z. C. Tu, “Elastic theory of membranes,” *AAPPS Bull* **16**, 30–33 (2006).
- [25] F. Campelo, C. Arnarez, S. J. Marrink, and M. M. Kozlov, “ Helfrich model of membrane bending: from gibbs theory of liquid interfaces to membranes as thick anisotropic elastic layers,” *Adv. Colloid Interface Sci.* **208**, 25–33 (2014).
- [26] I. Khmelinskii and V. I. Makarov, “On the effects of mechanical stress of biological membranes in modeling of swelling dynamics of biological systems,” *Sci Rep* **10**, 8395 (2020).
- [27] S. Skulj, Z. Brkljaca, and M. Vazdar, “Molecular dynamics simulations of the elusive matrix-open state of mitochondrial adp/atp carrier,” *Israel Journal of Chemistry* **60**, 1–10 (2020).
- [28] A. A. Oliveira, T. Rog, A. B. F. da Silva, R. E. Amaro, M. S. Johnson, and P. A. Postila, “Examining the effect of charged lipids on mitochondrial outer membrane dynamics using atomistic simulations,” *Biomolecules* **12**, 183 (2022).
- [29] Blake A. Wilson, Arvind Ramanathan, and Carlos F. Lopez, “Cardiolipin-dependent properties of model mitochondrial membranes from molecular simulations,” *Biophysical Journal* **117**, 429–444 (2019).
- [30] Weria Pezeshkian, Melanie König, T.A. Wassenaar, and Siewert Marrink, “Backmapping triangulated surfaces to coarse-grained membrane models,” *Nature Communications* **11**, 2296 (2020).
- [31] Susanne E. Horvath and Günther Daum, “Lipids of mitochondria,” *Progress in Lipid Research* **52**, 590–614 (2013).
- [32] D. Armstrong, *Lipidomics: Methods and Protocols* (Humana Press, Totowa, New Jersey, 2009).
- [33] Günther Daum and Jean E. Vance, “Import of lipids into mitochondria,” *Progress in Lipid Research* **36**, 103–130 (1997).
- [34] Ruud Hovius, José Thijssen, Peter van der Linden, Klaas Nicolay, and Ben de Kruijff, “Phospholipid asymmetry of the outer membrane of rat liver mitochondria: Evidence for the presence of cardiolipin on the outside of the outer membrane,” *FEBS Letters* **330**, 71–76 (1993).
- [35] Anton I.P.M de Kroon, Danièle Dolis, Andreas Mayer, Roland Lill, and Ben de Kruijff, “Phospholipid composition of highly purified mitochondrial outer membranes of rat liver and *Neurospora crassa*. is cardiolipin present in the mitochondrial outer membrane?” *Biochimica et Biophysica Acta (BBA) - Biomembranes* **1325**, 108–116 (1997).
- [36] Michael C.J. Chang and Betty I. Roots, “The lipid composition of mitochondrial outer and inner membranes from the brains of goldfish acclimated at 5 and 30c,” *Journal of Thermal Biology* **14**, 191–194 (1989).
- [37] A. Colbeau, J. Nachbaur, and P.M. Vignais, “Enzymac characterization and lipid composition of rat liver subcellular membranes,” *Biochimica et Biophysica Acta (BBA) - Biomembranes* **249**, 462–492 (1971).
- [38] Jane Comte, Bernard Maïsterrena, and Danièle C. Gautheron, “Lipid composition and protein profiles of outer and inner membranes from pig heart mitochondria. comparison with microsomes,” *Biochimica et Biophysica Acta (BBA) - Biomembranes* **419**, 271–284 (1976).
- [39] Jeffery B. Klauda Sunhwan Jo, Joseph B. Lim and Wonpil Im, “Charmm-gui membrane builder for mixed bilayers and its application to yeast membranes,” *Biophysical Journal* **97**, 50–53 (2009).
- [40] J. Huang, S. Rauscher, G. Nawrocki, T. Ran, M. Feig, B. L. de Groot, H. Grubmuller, and A. D. MacKerell Jr., “Charmm36m: an improved force field for folded and intrinsically disordered proteins,” *Nat Methods*. **14**, 71 (2017).
- [41] E. Lindahl, B. Hess, and D. van der Spoel, “Gromacs 3.0: A package for molecular simulation and trajectory analysis,” *J. Mol. Mod.* **7**, 306–317 (2001).
- [42] M. Parrinello and A. Rahman, “Polymorphic transitions in single crystals: A new molecular dynamics method,” *J. Appl. Phys.* **52**, 7182–7190 (1981).
- [43] S. Nose, “A molecular dynamics method for simulations in the canonical ensemble,” *Mol. Phys.* **52**, 255–268 (1984).
- [44] W. G. Hoover, “Canonical dynamics: Equilibrium phase-space distributions,” *Phys. Rev. A* **31**, 1695–1697 (1985).
- [45] T. Darden, D. York, and L. Pedersen, “Particle mesh Ewald: An N·log(N) method for Ewald sums in large systems.” *J. Chem. Phys.* **98**, 10089–10092 (1993).
- [46] William J. Allen, Justin A. Lemkul, and David R. Bevan, “Gridmat-md: A grid-based membrane analysis tool for use with molecular dynamics,” *Journal of Computational Chemistry* **30**, 1952–1958 (2009).
- [47] Louic Vermeer, Bert de Groot, Valérie Reat, Alain Milon, and Jerzy Czaplicki, “Acyl chain order parameter profiles in phospholipid bilayers: Computation from molecular dynamics simulations and comparison with h-2 nmr experiments,” *European biophysics journal : EBJ* **36**, 919–31 (2007).
- [48] A. A. Gurtovenko and I. Vattulainen, “Calculation of the electrostatic potential of lipid bilayers from molecular dynamics simulations: Methodological issues,” *J. Chem. Phys.* **130**, 06B610 (2009).
- [49] Z. A. Levine, R. M. Venable, M. C. Watson, M. G. Lerner, J. E. Shea, R. W. Pastor, and F. L. H. Brown, “Determination of biomembrane bending moduli in fully atomistic simulations,” *J. Am. Chem. Soc.* **136**, 13582 (2014).
- [50] M. C. Watson, E. S. Penev, P. M. Welch, and F. L. H. Brown, “Thermal fluctuations in shape, thickness, and molecular orientation in lipid bilayer,” *J. Chem. Phys.* **135**, 244701 (2011).
- [51] M. C. Watson, E. G. Brandt, P. M. Welch, and F. L. H. Brown, “Determining biomembrane bending rigidities from simulations of modest size,” *Phys. Rev. Letts* **109**, 028102 (2012).
- [52] H. L. Nguyen, V. H. Man, M. S. Li, P. Derreumaux, J. Wang, and P. H. Nguyen, “Elastic moduli of normal and cancer cell membranes revealed by molecular dynamics simulations,” *Phys. Chem. Chem. Phys.* **24**, 6225–6237 (2022).
- [53] L. T. Mai, H. T. Nguyen, P. Derreumaux, and

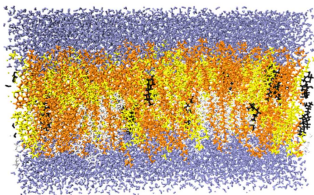
- P. H. Nguyen, "Structure and elasticity of healthy and alzheimer's disease cell membranes revealed by molecular dynamics simulations," *Proteins* (2023).
- [54] O. H. Ollila, H. J. Risselada, M. Louhivuori, E. Lindahl, I. Vattulainen, and S. J. Marrink, "3d pressure field in lipid membranes and membrane-protein complexes," *Phys. Rev Lett.* **102**, 078101 (2009).
- [55] J. M. Vanegas, A. Torres-Sanchez, and M. Arroyo, "Importance of force decomposition for local stress calculations in biomembrane molecular simulations," *J. Chem. Theor. Comput.* **10**, 691 (2014).
- [56] A. Torres-Sanchez, J. M. Vanegas, and M. Arroyo, "Examining the mechanical equilibrium of microscopic stresses in molecular simulations," *Phys. Rev. Lett.* **114**, 258102 (2015).
- [57] S. Park, A. H. Beaven, J. B. Klauda, and W. Im, "How tolerant are membrane simulations with mismatch in area per lipid between leaflets?" *J. Chem. Theory Comput.* **11**, 3466 (2015).
- [58] D. S. Patel, S. Park, E. L. Wu, M. S. Yeom, G. Widmalm, J. B. Klauda, and W. Im, "Influence of ganglioside gm1 concentration on lipid clustering and membrane properties and curvature," *Biophys J* **111**, 1987 (2016).
- [59] K. D. Wildermuth, V. Monje-Galvan, L. M. Warburton, and J. B. Klauda, "Effect of membrane lipid packing on stable binding of the alps peptide," *J. Chem. Theory Comput.* **15**, 1418–1429 (2019).
- [60] S. W. I. Siu, R. Vacha, P. Jungwirth, and R. A. Boeckmann, "Biomolecular simulations of membranes: Physical properties from different force fields," *J. Chem. Phys.* **128**, 125103 (2008).
- [61] J. B. Klauda, R. M. Venable, J. A. Freites, J. W. O'Connor, D. J. Tobias, C. Mondragon-Ramirez, I. Vorobyov, A. D. MacKerell, Jr., and R. W. Pastor, "Update of the charmm all-atom additive force field for lipids: Validation on six lipid types," *J. Phys. Chem. B* **114**, 7830 (2010).
- [62] M. Orsi and J. W. Essex, "Physical properties of mixed bilayers containing lamellar and nonlamellar lipids: insights from coarse-grained molecular dynamics simulations," *Faraday Discuss.* **161**, 249 (2013).
- [63] Y. Liu and J. F. Nagel, "Diffuse scattering provides material parameters and electron density profiles of biomembranes," *Phys. Rev. E* **69**, 040901 (2004).
- [64] N. Kucerka, J. F. Nagle, J. N. Sachs, S. E. Feller, J. Pencer, A. Jackson, and J. Katsaras, "Lipid bilayer structure determined by the simultaneous analysis of neutron and x-ray scattering data," *Biophys J.* **95**, 2356 (2008).
- [65] L. Wang, "Implications of the membrane dipole potential," *Annu. Rev. Biochem.* **81**, 615 (2012).
- [66] G. Daum, "Lipids of mitochondria," *Biochim. Biophys. Acta* **822**, 1 (1985).
- [67] T. Rog, H. Martinez-Seara, N. Munck, M. Oresic, M. Karttunen, and I. Vattulainen, "Role of cardiolipins in the inner mitochondrial membrane: Insight gained through atom-scale simulations," *J. Phys. Chem. B* **113**, 3413 (2009).
- [68] S. Poyry, T. Rog, M. Karttunen, and I. Vattulainen, "Mitochondrial membranes with mono- and divalent salt: Changes induced by salt ions on structure and dynamics," *J. Phys. Chem. B* **113**, 15513 (2009).
- [69] N. Khalifat, J. B. Fournier, M. I. Angelova, and N. Puff, "Lipid packing variations induced by ph in cardiolipin-containing bilayers: the driving force for the cristae-like shape instability," *Biochim. Biophys. Acta.* **1808**, 2724 (2011).
- [70] M. Frias, M. G. K. Benesch, R. N. A. H. Lewis, and R. N. McElhaney, "On the miscibility of cardiolipin with 1,2-diacyl phosphoglycerides: binary mixtures of dimyristoylphosphatidylethanolamine and tetramyristoylcardiolipin," *Biochim Biophys Acta.* **1808**, 774 (2011).
- [71] O. Domenech, A. Morros, M. E Cabanas, M. T. Montero, and J. Hernandez-Borrell, "Thermal response of domains in cardiolipin content bilayers," *Ultramicroscopy* **107**, 943 (2007).
- [72] Òscar Domènech, Fausto Sanz, M. Teresa Montero, and Jordi Hernández-Borrell, "Thermodynamic and structural study of the main phospholipid components comprising the mitochondrial inner membrane," *Biochimica et Biophysica Acta (BBA) - Biomembranes* **1758**, 213–221 (2006).
- [73] S. Sennato, F. Bordini, C. Cametti, C. Coluzza, A. Desideri, and S. Rufini, "Evidence of domain formation in cardiolipin-glycerophospholipid mixed monolayers. a thermodynamic and afm study," *J. Phys. Chem. B* **109**, 15950 (2005).
- [74] Alexander L. Boscia, Bradley W. Treece, Dariush Mohammadyani, Judith Klein-Seetharaman, Anthony R. Braun, Tsjerk A. Wassenaar, Beate Klösgen, and Stephanie Tristram-Nagle, "X-ray structure, thermodynamics, elastic properties and md simulations of cardiolipin/dimyristoylphosphatidylcholine mixed membranes," *Chemistry and Physics of Lipids* **178**, 1–10 (2014).
- [75] E. Beltran-Heredia, F.-C. Tsai, S. Salinas-Almaguer, F. J. Cao, P. Bassereau, and F. Monroy, "Membrane curvature induces cardiolipin sorting," *Commun Biol.* **2**, 225 (2019).
- [76] K. J. Boyd, N. N. Alder, and E. R. May, "Buckling under pressure curvature based lipid segregation and stability modulation in cardiolipin-containing bilayers," *Langmuir* **33**, 6937 (2017).
- [77] A. Rupperecht, E. A. Sokolenko, V. Beck, O. Ninnemann, M. Jaburek, T. Trimbuch, S. S. Klishin, P. Jezek, V. P. Skulachev, and E. E. Pohl, "Role of the transmembrane potential in the membrane proton leak," *Biophys J.* **98**, 1503 (2010).
- [78] J. F. Nagle, M. S. Jablin, S. Tristram-Nagle, and K. Akabori, "What are the true values of the bending modulus of simple lipid bilayers?" *Chem. Phys. Lipids* **185**, 3 (2015).
- [79] J. Pan, X. Cheng, M. Sharp, C. S. Ho, N. Khadka, and J. Katsaras, "Structural and mechanical properties of cardiolipin lipid bilayers determined using neutron spin echo, small angle neutron and x-ray scattering, and molecular dynamics simulations," *Soft Matter* **11**, 130 (2015).
- [80] P. Mitchell, "Coupling of phosphorylation to electron and hydrogen transfer by a chemi-osmotic type of mechanism," *Nature* **191**, 144 (1961).
- [81] V. G. Almendro-Vedia, P. Natale, M. Mell, and S. Bonnaeu, "Nonequilibrium fluctuations of lipid membranes by the rotating motor protein flf0-atp synthase," *Proc. Natl. Acad. Sci. USA* **114**, 11291 (2017).
- [82] P. B. Canham, "The minimum energy of bending as a possible explanation of the biconcave shape of the human

red blood cell,” *Journal of Theoretical Biology* **26**, 61 (1970).

- [83] W. Helfrich, “Elastic properties of lipid bilayers: Theory and possible experiments,” *Zeitschrift für Naturforschung* **28c**, 693 (1973).

TOC Graphic

Outer mitochondrial membrane



Inner mitochondrial membrane

